Effect of Precipitation on Mechanical Properties in the β-Ti Alloy Ti-24Nb-4Zr-8Sn

James Coakley[a,b,*], Khandaker M Rahman[c], Vassili A Vorontsov[c], Masato Ohnuma[d], David Dye[c]

[a] *Northwestern University, Department of Materials Science and Engineering, Evanston, IL 60208-3108, USA*
[b] *Department of Materials Science and Metallurgy, University of Cambridge, Cambridge CB3 OF3, England*
[c] *Department of Materials, Imperial College, South Kensington, London SW7 2AZ, England*
[d] *Laboratory of Quantum Beam System Engineering, Hokkaido University, Sapporo 060-0808, Japan*

Abstract

Tensile testing and cyclic tensile loading measurements were performed on heat-treated samples of annealed Ti-2448 and cold-rolled Ti-2448. Quenching from above the β-transus produces an alloy that is highly superelastic, has ultra-low elastic modulus ($10-25$ GPa) and exhibits hysteresis on loading-unloading cycles. On repeated cycling the strain energy absorbed in each cycle decreases. Annealed Ti-2448 exhibits a stable hysteresis loop. Peaks from the α'' phase are observed in X-ray diffraction (XRD) patterns, thus the material is quite lean in β-stabilising additions. The alloy is shown to be highly unstable when heat-treated. A combination of small angle X-ray scattering (SAXS), transmission electron microscopy (TEM) and X-ray diffraction (XRD) was employed to relate the thermally induced microstructural evolution to the change in mechanical properties. A heat-treatment of 80 °C to the cold-rolled material precipitated the ω phase, causing embrittlement. Increasing the ageing temperature from 80 to 300 °C increased the stiffness, made the elastic regime more linear, and further embrittled the alloy. The low temperature heat-treatments precipitate both ω and α'' phases. A higher temperature ageing treatment at 450 °C increased the yield strength to over 1GPa and caused embrittlement, indicating co-precipitation of α and ω phases.

Key words: titanium alloys, phase transformation, electron microscopy, mechanical characterisation, X-ray diffraction, aging

1. Introduction

A number of metastable β-Ti alloys currently being developed for biomedical applications, such as Gum Metal (Ti-36Nb-3Zr-2Ta (wt.%)) [1] and Ti-2448 (Ti-24Nb-4Zr-8Sn (wt.%)) [2], exhibit exceptional mechanical properties. The alloys are developments of the Ti-Nb binary system, and are biocompatible, superelastic, possess low elastic moduli and a high strength-to-weight ratio. They show a non-linear elastic regime on loading and also show hysteresis in the loading-unloading cycle. These two properties are related to a reversible stress induced $\beta \rightarrow \alpha''$ phase transformation [3, 4].

While these alloys have been developed primarily for the biomedical industry, there are many more potential applications. A hysteresis loop in the loading-unloading cycle corresponds to energy absorption, thus it may be possible to employ the alloys as metal dampers. The metastable β-Ti alloys precipitate a number of phases prior to the stable $\alpha + \beta$ microstructure, dependent on composition, processing route and heat-treatments [5–8]. The most widely documented of these is the athermal ω phase that can precipitate on quenching [7–9], and the isothermal ω phase that forms from the athermal ω phase on subsequent low temperature ageing [7–9]. Relating the precipitation processes to the mechanical properties of these alloys is an area of ongoing research. Ikeda *et al.* attributed a large increase in hardness to the precipitation of isothermal ω phase in Ti-Mo [5]. Jones *et al.* attributed an increase in hardness of Gum Metal to fine scale α precipitation during low temperature ageing and not to the ω phase [6].

This study relates the deterioration of the mechanical properties of Ti-2448 to thermally and stress-induced changes of the microstructure. Mechanical testing data of Gum Metal are also presented for comparison. Ti-2448 is shown to be unstable, with changes in microstructure and a corresponding deterioration of mechanical properties observed at the lowest ageing temperature examined, 80 °C.

2. Experimental Details

2.1. Material Processing

The production route of the Gum Metal studied has previously been reported [7]. The final processing step was an extrusion to 12 mm bar. Two plates of Ti-2448 were supplied from the Chinese Academy of Science Institute of Metal Research, Shenyang National Laboratory for

*Corresponding Author. Tel: +1 312 774 8634; fax: +1 847 467 2269

Email address: james.coakley@northwestern.edu (James Coakley)

Table 1: Bulk compositions of the three β-Ti alloys used in this study, measured by inductively coupled plasma optical emission spectrometry (ICP-OES) and LECO analyses. All compositions are in weight % except for hydrogen (ppmw).

Element (wt.%)	H (ppmw)	Nb	O	Sn	Ta	Ti	Zr
Ti-2448 Ann	<10	21.4	0.11	8.0	-	Bal	3.9
Ti-2448 CR	20	21.6	0.07	7.3	-	Bal	3.9
Gum Metal	22	36.2	0.26	-	2.0	Bal	3.2

Materials Science. The first was cold-rolled to 90% strain (labelled CR), and the second was cold-rolled to 90% strain followed by an anneal at 700 °C/5 h (labelled Ann). The compositions of all samples were measured by ICP-OES and LECO analyses, and are presented in Table 1.

Samples that received further heat-treatments were encapsulated in an Argon atmosphere to inhibit oxidation and were water quenched following each heat-treatment. The heat-treatments applied to the Ti-2448 samples are shown in Table 2, along with the nomenclature employed throughout this paper and mechanical testing results that are discussed in the Results section. The Ti-2448 samples discussed are annealed (Ann), cold-rolled (CR) and water quenched after being held above the β-transus at 1000 °C/1 h, *i.e.* beta-quenched (BQ). Subsequent heat-treatments were performed on these conditions and air-cooled (e.g CR 125 °C/24 h). Finally a cold-rolled condition that received a dual heat-treatment of 300 °C/4 h + 450 °C/4 h is denoted CR DHT.

2.2. Mechanical Testing

Small dog bone geometry specimens with gauge dimensions of 1.5×2×19 mm were fabricated by electric discharge machining (EDM). Room temperature tensile testing and cyclic loading experiments were performed on 5 kN and 100 kN Zwick-Roell static load frames. The tensile testing strain rate was $\dot{\varepsilon} = 10^{-3}\text{s}^{-1}$ and cyclic loading-unloading cycles were performed at $\dot{\varepsilon} = 2.5 \times 10^{-3}\text{s}^{-1}$. In addition, the cyclic loading of Gum Metal was performed on an Instron servohydraulic thermomechanical fatigue (TMF) rig with 5 mm diameter round samples and a frequency range of 0.05 Hz − 10 Hz was examined.

2.3. X-Ray Diffraction (XRD)

Laboratory XRD was performed on five specimens that were selected based on the mechanical testing results. The samples measured were (i) Ann, (ii) CR, (iii) BQ, (iv) CR 80 °C/750 h, and (v) CR 250 °C/24 h. The measurements were performed on a Rigaku Ultima IV XRD instrument using Cu-K$_\alpha$ X-ray radiation with a characteristic wavelength of 1.541Å at 40kV and 20mA current. Data were collected over a range of 30 - 100° 2θ. Phase identification was performed by comparison to powder patterns using CrystalDiffract software.

2.4. Small Angle X-Ray Scattering (SAXS)

SAXS measures the shape and intensity of the coherent elastic scattering at small angles from the incident beam.

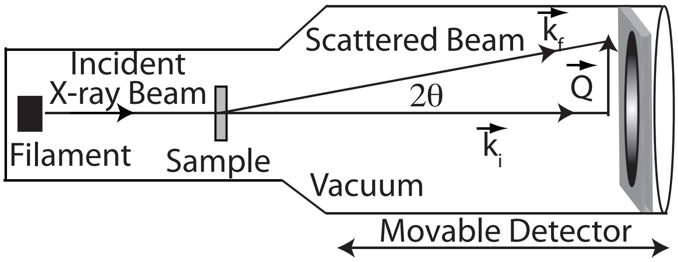

Figure 1: Schematic of the experimental arrangement used to perform small angle X-ray scattering at Hokkaido University.

The angles are much smaller than classical diffraction angles [12–19], typically under 5 °. Pinhole SAXS can provide scattering patterns from structures or fluctuations in composition or density on the length scale of about 1 to 100 nm, corresponding to the size of smaller precipitates in engineering alloys. SAXS measurements were performed on all CR samples presented in Table 2 except the DHT condition.

A schematic of laboratory small angle X-ray scattering (lab-SAXS) is shown in Figure 1. $\mathbf{k_i}$ is the incident wave vector with magnitude $k = 2\pi/\lambda$. The scattering vector $\mathbf{Q}$ is the difference between incident and scattered wave vectors $\mathbf{Q} = \mathbf{k_f} - \mathbf{k_i}$. The magnitude of Q quantifies the lengths of the reciprocal space $Q = \frac{4\pi}{\lambda}\sin\theta$, where 2θ is the scattering angle. Thus, smaller particles are observed at larger Q in reciprocal space.

The SAXS instrument at Hokkaido University is a high-flux/high-transmission Mo Kα ($\lambda = 0.07$ nm) system with a two-dimensional confocal mirror (Rigaku Nanoviewer) and a two-dimensional movable detector (Pilatus 100K) that can probe a Q-region of about $0.2 - 10\,\text{nm}^{-1}$, all within vacuum at room-temperature. The beam diameter at the sample position is <1mm. SAXS measurements were performed in both long and short detector distance configurations, with sample-to-detector distances of approximately 1360 mm and 350 mm respectively. Sample measurement times varied from 4 − 10 h. The thicknesses of the SAXS samples at the point of X-ray irradiation were determined from the transmission rates (the ratio of the attenuated direct beam measurements with and without a sample mounted) according to the equation $T_s(\lambda) = \exp(-\mu_s t_s)$, where μ_s and t_s are the line absorption factor of the sample for X-rays and sample thickness respectively. Using the sample composition and the line absorption factor for constituent elements, μ_s can be determined, thereby determining sample thickness t_s. Reduction of the data to absolute scattering probabilities $\partial\Sigma(Q)/\partial\Omega$ was performed using the Nika package of Argonne National Laboratory [10]. The beam center was determined by measurement of a silver behenate standard. Data were corrected for transmissions $T(\lambda)$ measured with the central beam stop removed and the incident beam attenuated, for backgrounds from the empty furnace, and for dark current background in the detector. Data were

Table 2: The Young's modulus E of the β-Ti alloys examined with various heat-treatments (HT) in the stress ranges of $50-400$ MPa, $400-600$ MPa, and $50-600$ MPa. The estimated yield stress σ_{y}, corresponding yield strain ε_{y}, and failure strain ε_{f} are presented. A sample of cross-rolled Ti-6Al-4V was measured as a standard material. Ti-2448 CR DHT received a dual heat-treatment of 300 °C/4 h + 450 °C/4 h with quenching after each heat-treatment (HT).

Alloy + HT	Nomenclature	E (GPa) $\sigma_{\mathrm{range}} = 50-400$ MPa	E (GPa) $400-600$ MPa	E (GPa) $50-600$ MPa	σ_{y} (MPa)	ε_{y} (%)	ε_{f} (%)
Ti-6Al-4V		101	100	100	860	0.9	16.7
Gum Metal	Gum	56	27	40	830	2.8	13.0
Ti-2448 Ann	Ann	48	16	28	640	2.6	13.8
Ti-2448 Ann + 125 °C/96 h	Ann 125 °C/96 h	56	26	40	610	1.5	9.5
Ti-2448 Ann + 300 °C/24 h	Ann 300 °C/24 h	64	48	58	710	1.2	10.3
Ti-2448 Ann + 1000 °C/1 h	BQ	25	10	16	625	3.8	11.8
Ti-2448 CR	CR	58	41	45	750	1.8	6.1
Ti-2448 CR + 80 °C/24 h	CR 80 °C/24 h	53	40	48	750	1.7	4.0
Ti-2448 CR + 125 °C/24 h	CR 125 °C/24 h	58	44	52	800	1.8	2.7
Ti-2448 CR + 150 °C/24 h	CR 150 °C/24 h	56	46	52	850	1.9	2.4
Ti-2448 CR + 250 °C/24 h	CR 250 °C/24 h	57	61	59	900	2.1	1.7
Ti-2448 CR + 80 °C/750 h	CR 80 °C/750 h	52	34	44	600	1.2	2.9
Ti-2448 CR + 450 °C/24 h	CR 450 °C/24 h	78	81	79	1020	1.4	1.7
Ti-2448 CR DHT	DHT	80	77	79	860	1.2	1.2

placed on the absolute scale by measuring a glassy carbon sample as an absolute intensity calibration standard [11].

The probability of small angle X-ray scattering from uniform monodisperse particles is

$$\frac{\partial \Sigma(Q)}{\partial \Omega} = NV^2(\Delta\rho)^2 P(Q) + \mathrm{BKG} \qquad (1)$$

where N is the number of particles per unit volume, V is the volume of one particle, and $P(Q)$ is the particle form factor or shape function. Note that the dispersed particle volume fraction $\phi = NV$. $P(Q)$ depends on the size and shape of the particle and is normalised such that $P(Q = 0) = 1.0$ [20]. BKG is any residual background not allowed for in the data reduction, often a flat term for incoherent scattering from certain elements. $\Delta\rho = \rho_{\mathrm{ppt}} - \rho_{\mathrm{matrix}}$ is the X-ray scattering length density difference between the particle and its matrix. The scattering length density of phase x is

$$\rho_x = (\rho_{\mathrm{mass}} N_A / M_r) \Sigma n_i b_i \qquad (2)$$

where ρ_{mass} is the phase mass density, N_A is Avogadro's number, M_r is the molecular weight of the phase, n_i is the atomic fraction of element i in the phase, and b_i is that element's associated X-ray scattering length. The scattering lengths of X-rays are proportional to atomic number, unlike neutrons that vary erratically across the periodic table.

2.5. Transmission Electron Microscopy (TEM)

TEM was performed on CR, CR 80 °C/750 h and CR 250 °C/24 h. These conditions were again chosen following the mechanical testing, to investigate the microstructural evolution that altered the Young's modulus and ductility.

Specimens for TEM analysis were removed by spark-erosion and thinned using twin-jet electropolishing in a solution of 8 vol.% H_2SO_4 in methanol at −40°C and 18 V. TEM foils were examined using a JEOL JEM 2000FX microscope at 200kV.

3. Results

3.1. Tensile Testing

Figure 2a shows the tensile test results of the alloys in their initial conditions (Gum, Ti-2448 Ann and CR). The kinks in the plastic regime are from holding and releasing the cross-head position in order to remove the extensometer. A Ti-6Al-4V cross-rolled sample is also presented as a standard alloy to illustrate the low elastic moduli of the β-Ti alloys. The beta-quenched sample and a typical ω age heat-treatment (300 °C/24 h) of Ti-2448 are also shown. Obbard *et al.* previously illustrated that an increasing oxygen content in Ti-2448 increases the Young's modulus and strength of the alloy [2]. Referring to Table 1, Gum Metal has a higher oxygen content than the Ti-2448 alloys, which will contribute to a higher Young's modulus and strength. Ti-2448 CR did not receive the 700 °C/5 h anneal that the Ti-2448 Ann sample was exposed to, thus the Ti2448 CR has higher strength but is brittle. The beta-quenched material exhibits the highest super-elasticity, while the ω aged sample possesses a very linear elastic region and is stiffer.

The effect of low temperature ageing on Ti-2448 CR is shown in Figure 2b. A heat-treatment as low as 80 °C/24 h is seen to increase the elastic modulus and reduce the ductility. The elastic regime becomes increasingly linear and stiffer with increasing heat-treatment temperature and the failure regime becomes more brittle, with the 250 °C sample fracturing prior to yield.

Although not presented here, low temperature ageing (200 °C/9 h) of β-quenched Ti-2448 sample exhibited the same trends on mechanical properties as low temperature ageing of the CR material, with an increase in material brittleness and stiffness. Heat-treating Ti-2448 Ann at 125 °C also had the same effect.

Following the unexpected result whereby the mechanical properties changed with a heat-treatment as low as

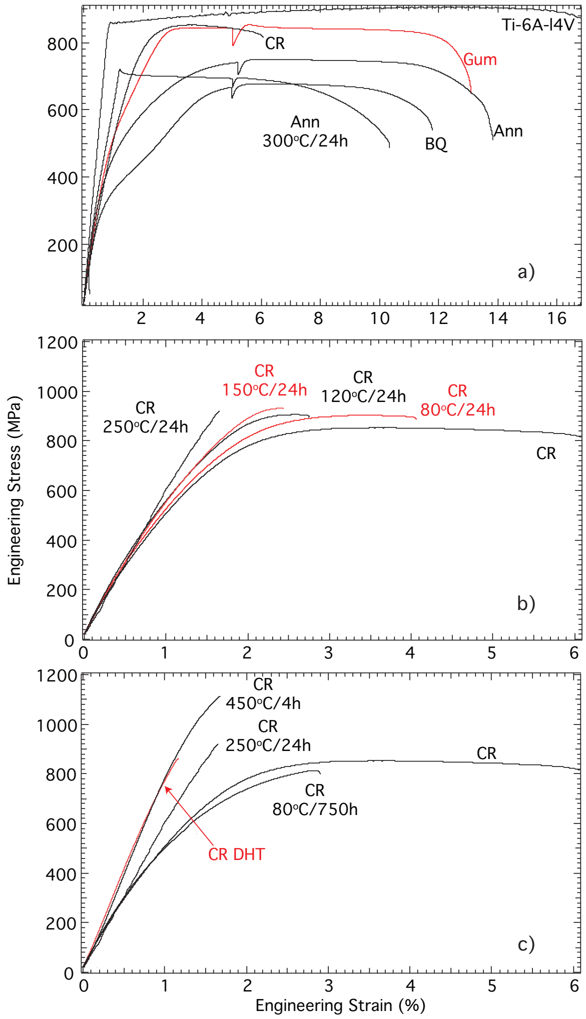

Figure 2: a) Tensile test curves of Ti-2448 Ann, Ti-2448 CR and Gum Metal in the initial conditions. The change in tensile properties of Ti-2448 is dramatic following a beta-quench (BQ), and also following a low temperature age (Ann 300 °C/24 h). b) The change in tensile properties of Ti-2448 CR following 1 day of low temperature heat-treatments between 80 °C – 250 °C. c) The effect of various heat-treatments on the tensile properties of Ti-2448 CR. All tests were to failure.

80 °C/24 h, a longer age of 80 °C/750 h was tested to confirm this observation, and is presented in Figure 2c. The elastic regime of CR 80 °C/750 h was very similar to that of CR, however it failed at 2.9% while the CR sample fails at 6.1% strain, Table 2. Two further heat-treatments were performed and are presented. The first was a 450 °C/4 h heat-treatment in order to precipitate the α phase. Given the brittleness of the alloy, it appears that $\alpha + \omega$ phases have co-precipitated, which was the case for a 400 °C/16 h heat-treatment performed on Gum Metal [7]. The alloy was stiffer than the CR 250 °C/24 h (79GPa and 59GPa respectively) and had a much higher yield strength, Table 2. The final heat-treatment studied was a dual heat treatment (DHT) of Ti-2448 CR + 300 °C/24 h + 450 °C/4 h, in order to investigate the effect of an ω age followed by an α age. The stiffness was the same as the one step 450 °C/4 h exposure, but the yield point was at a much lower stress (860 vs. 1020MPa), and both samples fractured at yield.

3.2. Cyclic Loading

The effects of heat-treatment, maximum stress, and number of cycles during repeated loading-unloading are presented in Figure 3. Both Figures 3d - f and and j - k suggest a minimum threshold stress is required to complete the stress-induced transformation to obtain hysteresis. On cycling, whilst the the hysteresis loops narrow and the minimum stress decreases in value, a hysteresis loop remains. The annealed samples exhibited no hysteresis in the loading-unloading cycle when cycled between 50 – 200 MPa, 50 – 250 MPa, 50 – 350 MPa and 50 – 400 MPa, Figures 3a - d. They exhibited a very slight hysteresis loop during 50 – 500 MPa cycles (Figure 3e). The cyclic loading-unloading between 50 – 600 MPa showed a relatively large hysteresis loop that was stable, being present after 200 cycles (Figure 3f). The annealed sample +300 °C/24 h HT showed no hysteresis in the loading-unloading cycles between 50 – 500 MPa and 50 – 600 MPa, Figures 3g - j. The alloy is stiffer and the elastic region is more linear (58 vs. 28GPa).

The BQ sample exhibited a large hysteresis loop during a loading-unloading cycle up to both 500 and 600 MPa, however the hysteresis loop was not stable, and had closed after 200 cycles (3k - l). The elastic loading response is a different shape in the 1st cycle and 200th cycle. This alloy would presumably show hysteresis at a lower stress, based on the shape of the loading-unloading curve in Figure 3k.

The first 50 cycles of loading-unloading of Gum Metal were performed at 0.05 Hz on a TMF rig, and the frequency was stepped every 50 cycles until a frequency of 10 Hz was reached in the final 50 cycles (cycles 550 - 600). No hysteresis was seen in any of the loading-unloading cycles between 50 – 500 MPa, 3j. The first loading-unloading cycle between 50 – 700 MPa exhibited a clear hysteresis loop, however after 5 cycles this hysteresis loop had decreased in size, and is barely evident in the 50th cycle, 3j. The cycles up to the 600th cycle are not shown on this curve, but lay over the 50th cycle with very little hysteresis evident. The cyclic loading response of Gum Metal is very different to that of Ti-2448, and it is interesting to note that a non-linear elastic regime does not necessarily mean a hysteresis loop will occur on loading-unloading, see for example cycle 50 in Figure 3j.

There is an accumulation of strain during the cyclic loading of Ti-2448, Figure (3a - l), observed as an increase in strain with cycle number at each minimum stress. This phenomenon has been noted before, most recently in Gum metal and TWIP steel [21–23].

3.3. Small Angle X-ray Scattering (SAXS)

The small angle scattering from the CR material was isotropic, and the data were fully reduced and azimuthally averaged. Selected SAXS results are presented in Figure 4, along with model fits. The model is presented in

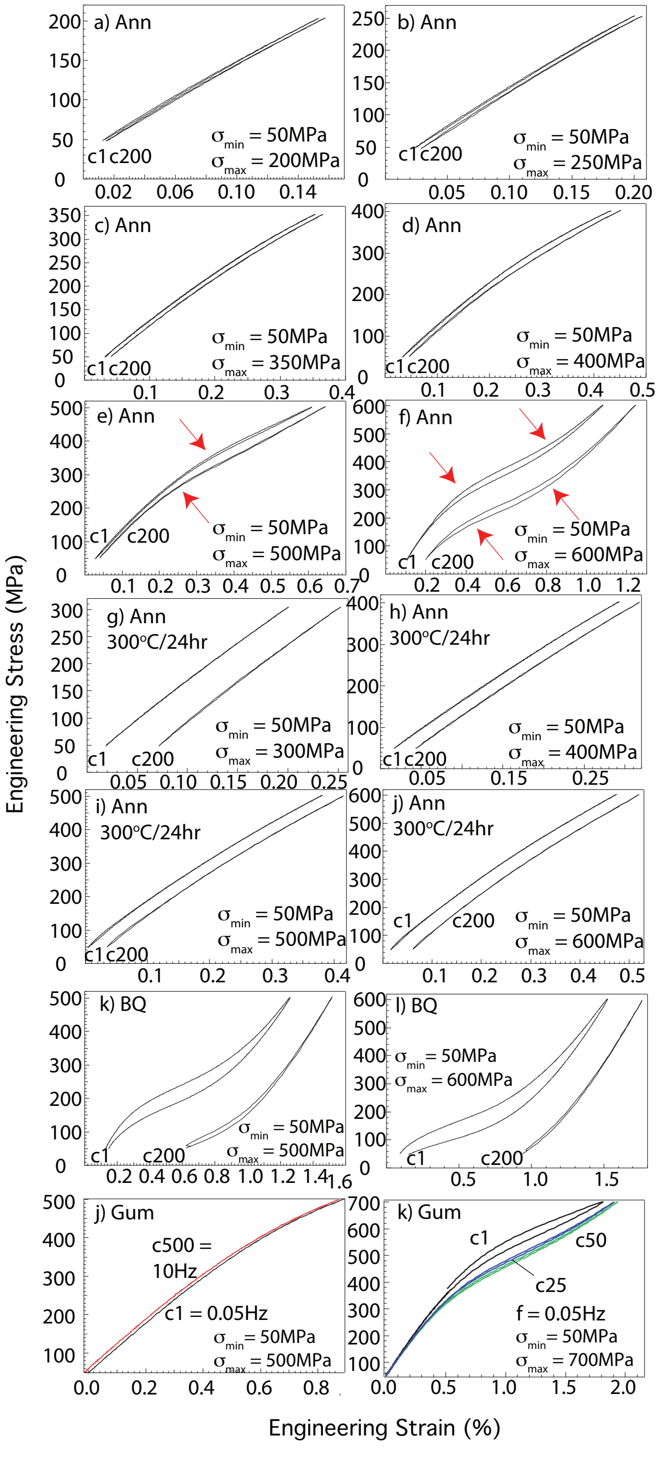

Figure 3: The 1st (c1) and 200th (c200) loading cycle at room temperature of a) - f) Ti-2448 Annealed, g) - j) Ti-2448 Annealed + 300 °C/24 h, k) - l) Ti-2448 beta-quenched (BQ), all at room temperature. The minimum and maximum stresses are shown on each graph, and the strain rate was $2.5 \times 10^{-3}\mathrm{s}^{-1}$. j - k) Cyclic loading of Gum Metal on a TMF rig. The decrease of the stresses with cycling at the beginning and end of the phase transformation are highlighted by red arrows, as guides to the eye.

the Discussion section. Error bars have been included on the Ti-2448 CR 250 °C/24 h data, but have been removed

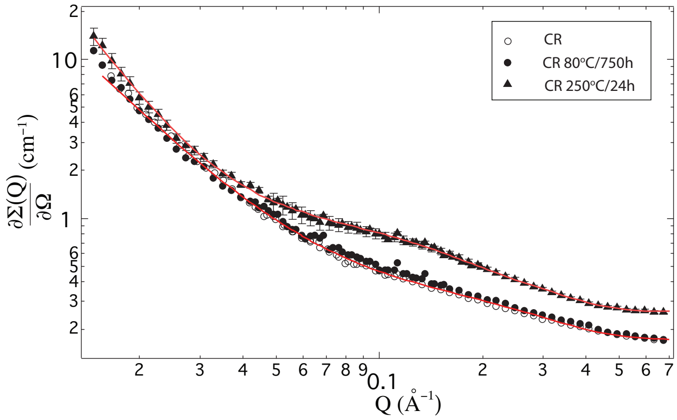

Figure 4: SAXS measurements of Ti-2448 CR, Ti-2448 CR 80 °C/750 h, and Ti-2448 CR 250 °C/24 h. Model Fits to CR and CR 250 °C/24 h are shown with a solid red line.

from the other measurements as they obscure the data. For the Ti-2448 CR measurement, there was a change in slope at $Q \sim 0.063\text{Å}^{-1}$ which is indicative of nanoscale precipitates. CR 80 °C/31 days lies almost directly over the non heat-treated sample, such that the micrsostructural changes that have altered the mechanical properties are too subtle to be identified by SAXS. Although not presented, the heat-treatments up to 150 °C/24 h show no obvious deviation from the initial Ti-2448 CR measurement. However after 250 °C/24 h heat-treatment there was a slight increase in intensity between $Q \sim 0.063 - 0.28\text{Å}^{-1}$. As the graph is a log-log plot, the higher intensity of this measurement at high Q is exaggerated. It is apparent that a nanoscale precipitation process is occurring during this heat-treatment, and modelling was employed to extract the precipitate size and shape. It is interesting to note that the change in slope of Ti-2448 CR occurs at $Q \sim 0.063\text{Å}^{-1}$, and the increase in intensity of CR 250 °C/24 h occurs in the region of $Q \sim 0.063 - 0.28\text{Å}^{-1}$.

3.4. X-ray Diffraction (XRD)

XRD patterns are presented in Figure 5 for (i) Annealed and BQ samples, and (ii) CR, CR +250 °C/24 h and CR +80 °C/750 h samples. Phase identification was performed by comparison to powder patterns using CrystalDiffract software with the following lattice parameters: α'' of a Ti-Mo based alloy [24], α of Ti-5553 [25], ω of pure Ti [26], and β values were estimated as $a \sim 3.30$Å. Due to extensive overlapping of peak positions it is not trivial to attribute the diffraction peaks to the appropriate crystal structure. Although XRD has been used to study precipitation processes in β-Ti alloys. It should only be used to provide initial insight, as ω and α reflections may be lost in the background. TEM diffraction or synchrotron diffraction should be used for definitive characterisation [27–32].

The compound peaks around the β peaks of the annealed sample suggest that α may be present, Figure 5i(b).

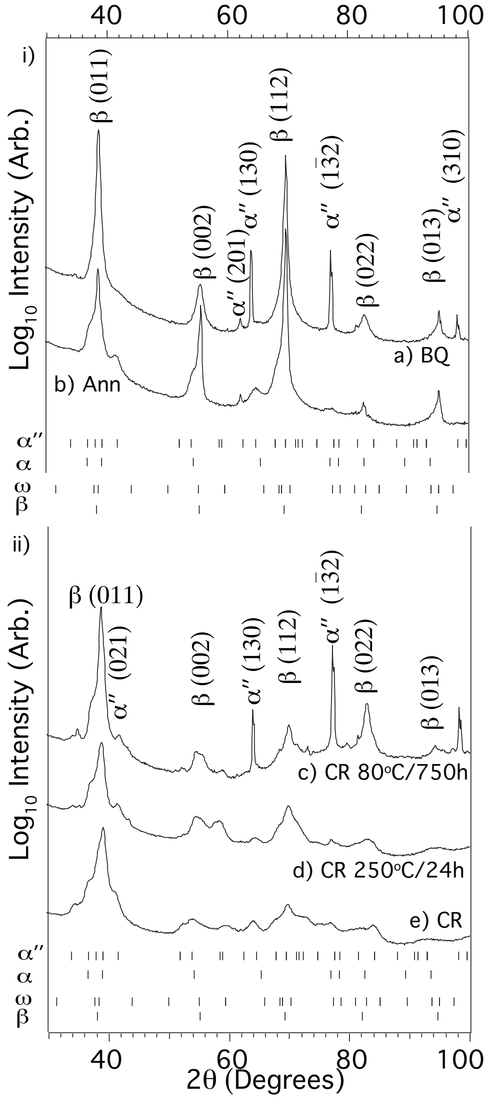

Figure 5: X-ray diffraction data of Ti-2448 in i-a) the beta-quenched condition (BQ), i-b) annealed (Ann) condition, ii-c) cold-rolled (CR) + 80 °C/750 h condition, ii-d) CR + 250 °C/24 h condition, and ii-e) CR condition. Peak positions and peak indexing are presented for α, β, α'' and ω.

The peaks labelled α'' (201), (130), and (1$\bar{3}$2) are associated with the α'' phase. The annealed material diffraction spectrum could be labelled fully by just considering the α'' and β phases.

β-quenching suppresses the peaks around the β (011), (002) and (112), which is perhaps indicative that α precipitates have been removed from the high temperature thermal exposure, Figure 5i(a). The α'' (201), (130) and (310) are very distinct and of high intensity.

The diffraction peaks of the CR sample are very broad and of low intensity, Figure 5ii(e) . The β peaks are much less distinct than in the annealed condition. There is no clear β (013) peak which may be due to texture induced from the rolling process [34]. The five peaks around the β (011) are typical of the α'' phase [33].

With heat-treatment at 250 °C the β peaks appear to become more distinct at (011), (112) and (022) reflections, Figure 5ii(d). It appears that the precipitate contributions around the β (011) diminish and the α'' peaks at higher angles are strong.

The difference in diffraction patterns of the CR 80 °C/750 h heat-treatment is dramatic for such a low temperature age, Figure 5ii(c). Similarly to the case of the beta-quench, peaks are present at 64.0, 74.2 and 98.3 ° that were not present prior to heat-treatment. These are associated with α'' (201), (130), and (1$\bar{3}$2). The multiple peaks around the β (011) are associated with the α'' phase.

3.5. Transmission Electron Microscopy (TEM)

Figure 6a shows a TEM diffraction pattern of the CR condition viewed parallel to the $<110>_\beta$ zone axis. A corresponding schematic showing the location of diffraction spots due to the α phase is presented in Figure 6b to aid interpretation of the diffraction pattern. Diffraction spots due to α'' phase, when present, appear at $1/2(112)_\beta$ positions. Thus, care needs to be taken when identifying reflections around the $1/2(112)_\beta$ positions as they may correspond to the α and/or the α'' phases. The ω phase reflections appear at $1/3(112)_\beta$ and a reflection due to the ω phase is highlighted in Figure 6a. A dark field image from $1/3(112)_\beta$ reflection is presented in Figure 6c. Nanoscale laths are observed, which are typical of the α phase [7]. By comparison of the diffraction pattern with the schematic, combined with the typical α lath morphology observed in dark field imaging using the $1/3(112)_\beta$ is evidence that at least some nanoscale α phase may be initially present in Ti-2448 CR. If this is indeed the alpha phase, the authors suggest it was nucleated prior to the cold-rolling process. It cannot be ruled out that these precipitates may be α'' which were strain induced during the cold-rolling process.

Figure 7a shows a TEM diffraction pattern of the CR 80 °C/750 h condition viewed parallel to the $<113>_\beta$ zone axis. Dark field images from the ω reflection highlighted are presented in Figure 7b and c. The diffraction pattern and dark-field images illustrate that extensive nanoscale ω precipitation has occurred. There are clear spots at $1/2(112)_\beta$ associated with the α'' phase.

Figure 8a shows a TEM diffraction pattern of the CR 250 °C/24 h condition viewed parallel to the $<110>_\beta$ zone axis. Diffraction spots at $1/3(112)_\beta$ due to the ω phase are observed, and one is highlighted. Dark field imaging clearly shows these particles are under 10 nm diameter and there is a high number density of precipitates, 8b. Comparing the diffraction patterns of CR 250 °C/24 h (Figure 8a) and CR (Figure 6a), the diffraction spots due to α are not present in the CR 250 °C/24 h diffraction pattern, but are very apparent in the Ti-2448 CR sample. Thus the heat-treatment has reduced the α concentration and increased the ω and α'' concentration. This is in agreement with the XRD data, Figure 5b(ii).

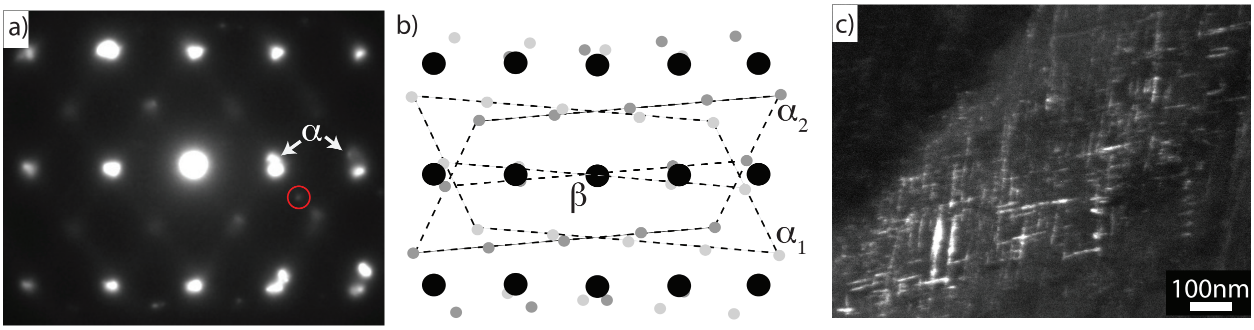

Figure 6: a) TEM diffraction pattern of Ti-2448 CR viewed parallel to the <110>$_\beta$ zone axis, with diffraction spots due to the α phase evident. Two α spots are labelled and an ω reflection is highlighted with a circle. b) Schematic illustrating α diffraction spot locations from two orientations on the <110>$_\beta$ zone axis (α: grey, β: black). c) Dark field imaging from the $\sim$1/3(112)$_\beta$ reflection associated with the ω phase.

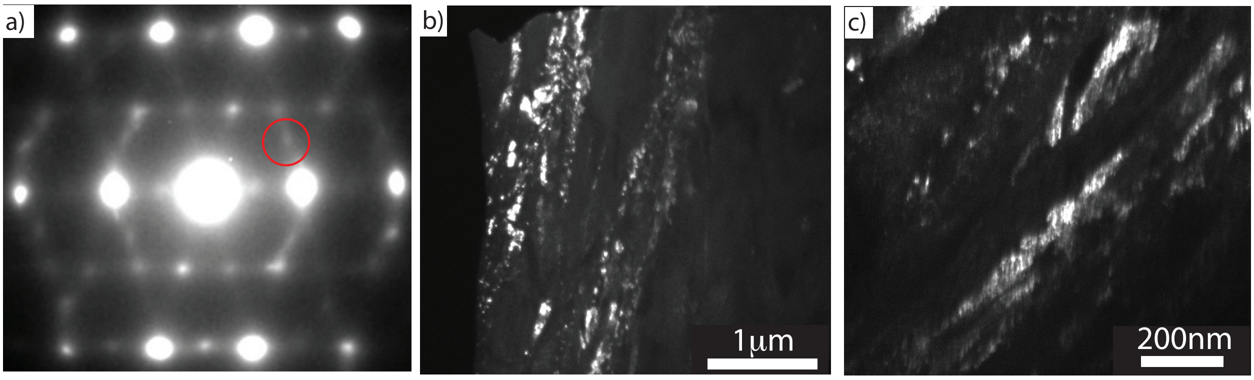

Figure 7: a) TEM diffraction pattern of Ti-2448 CR + 80 °C/750 h viewed parallel to the <113>$_\beta$ zone axis, with a diffraction spot due to the ω phase highlighted. b & c) Dark field imaging from the 1/3(112) reflection associated with the ω phase.

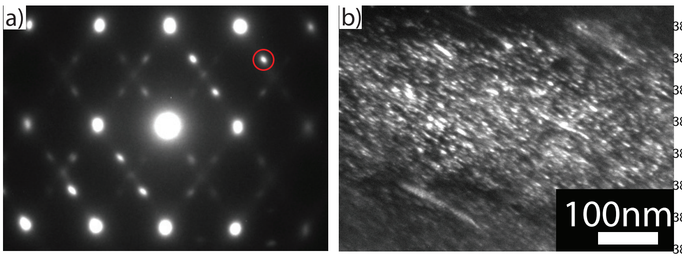

Figure 8: a) TEM diffraction pattern of Ti-2448 CR + 250 °C/24 h viewed parallel to the <110>$_\beta$ zone axis, with a diffraction spot due to the ω phase highlighted. b) Dark field imaging from the 1/3(112) reflection associated with the ω phase.

4. Discussion

4.1. SAXS Modelling

A SAXS model was developed using the FISH software package [35] in order to extract microstructual parameters from the SAXS measurements. The model is identical to a previously developed model that is discussed elsewhere in extensive detail [7], but without a structure factor S(Q). The model assumes that the scattering observed arose from nanoscale disc-shaped particles. This is reasonable for the CR 250 °C/24 h which has a high volume fraction of disc-shaped ω particles (Figure 8). For the case of CR which possesses both α phase laths and ω phase discs, it is assumed that scattering at the length-scale of $\sim$ 2nm is due to the ω phase only, which is also reasonable.

The model $\partial\Sigma(Q)/\partial\Omega = P(Q)_{\mathrm{disc}} + aQ^{-n} + \mathrm{BKG}$ fitted well to the data using a Marquadt iteration to minimise the least squares error, where $P(Q)_{\mathrm{disc}}$ is the form factor for monodisperse disc shaped particles, BKG is a flat background term to account for incoherent scattering, and aQ^{-n} accounts for scattering that arose from surface morphology. Although the model fits well to the data, it may not be a unique solution. The model fits are presented in Figure 4. The fitting parameter results for disc diameter D, disc length (*i.e.* thickness) L, and the $\phi(\Delta\rho)^2$ term are presented in Table 3. The model results are reasonable based on TEM.

The diameter of the precipitates is $\sim$ 1nm for CR and heat-treated Ti-2448 CR, Table 3. There is a small change in particle thickness from 2.4nm for Ti-2448 CR to 3.3nm for Ti-2448 CR 250 °C/24 h. The $\phi(\Delta\rho)^2$ term also increases. Presumably this is due to both (i) a volume fraction increase and (ii) a change in precipitate and matrix composition that alters the $\Delta\rho$ value. It is not possible to separate and quantify the contributions of ϕ and $\Delta\rho$ without complementary atom probe tomography, which is beyond the scope of this paper.

Table 3: SAXS model results from fitting of Ti-2448 CR and Ti-2448 CR 250 °C/24 h, where ϕ is the particle volume fraction, $\Delta\rho$ is the scattering length density contrast between precipitate and matrix, and D and L are the diameter and length of the disc shaped particles respectively.

Material	$\phi(\Delta\rho)^2$ 10^{-4} cm^{-4}	D nm	L nm
Ti-2448 CR	1.4	0.9	2.4
Ti-2448 CR 250 °C/24 h	2.0	1.2	3.3

4.2. Transmission Electron Microscopy (TEM)

Based upon the lath morphology of the precipitates it appears that the cold-rolled material initially possesses some α precipitates [7], Figure 6c. XRD data shows that α'' is initially present, Figure 5ii(e). The XRD data (Figure 5ii(c)) and TEM diffraction pattern (Figure 7a) of the Ti-2448 CR + 80 °C/750 h both show that the heat-treatment has precipitated ω and extensive α''. Similarly the CR +250 °C/24 h has also precipitated α'' with extensive ω precipitation, Figure 5ii(d) and Figure 8.

4.3. Tensile Testing and Cyclic Loading

Samples of cross-rolled Ti-6Al-4V were tensile tested to failure and cyclically loaded, to provide confidence in the testing methodology. Table 2 summarises the key mechanical testing data from tensile testing and Table 4 summarises the energy absorption during cyclic loading-unloading cycles for the samples studied. For Ti-6Al-4V, the loading and unloading curves lay perfectly over one another in the elastic region as expected so there was no hysteresis loop corresponding to strain energy absorption. The Young's modulus was 100 GPa. This falls within the lower limit of values between $100-120$GPa published for this material [36].

As many of the elastic regimes of the materials tested were non-linear, Figure 2, the stiffnesses are presented within stress bounds of $50-400$ MPa, $400-600$ MPa, and $50-600$ MPa. The stiffness of the BQ material is remarkably low and non-linear, between $\sim$ 25GPa and 10GPa depending on the stress bounds, Table 2. The non-linear elastic regime followed by a smooth progression into the plastic regime makes the identification of the yield point (σ_y, ε_y) from the tensile curve inherently difficult, while a 0.2% offset proof stress cannot be inferred from the elastic regime. In the samples which displayed this loading response the yield points are estimated. The β-quenched material is clearly superelastic, and the yield stress and strain are 625MPa and $\sim$ 3.8% respectively. The annealed material also shows a non-typical loading response, although they are less dramatic than the BQ material. The stiffness ranges between $48-16$ MPa, and it has a higher yield stress and is less superelastic, $\sigma_y \sim$ 640MPa and $\varepsilon_y \sim 2.6\%$. Ti-2448 Ann + 300 °C/24 h is much stiffer, more linear in the elastic regime and has a clear yield point, Figure 2. However the stiffness is still approximately half that of Ti-6Al-4V.

The area under a stress-strain curve corresponds to strain energy per unit volume. Thus if a hysteresis loop

Table 4: The strain energies absorbed during loading-unloading cycles U_{abs} for the 5th (c5) and 200th (c200) cycle from $50-500$ MPa and 600MPa are presented. The Gum Metal data, highlighted by *, was measured between $50-700$ MPa cycles. A sample of cross-rolled Ti-6Al-4V was measured as a standard material.

	U_{abs} c5 (%)	U_{abs} c200 (%)	U_{abs} c5 (%)	U_{abs} c200 (%)
σ_{range} (MPa)	50 - 500	50 - 500	50 - 600	50 - 600
Ti-6Al-4V	0	0	0	0
Gum	0	0	1*	1*
Ann	2	1	4	4
Ann 300 °C/24 h	0	0	0	0
BQ	10	1	11	1

occurs in the loading-unloading cycle, the area enclosed in the loop corresponds to strain energy absorption per unit volume. The fraction of strain energy absorbed $U_{\mathrm{abs}} = (U_L - U_{UL})/U_L$ where U_L is the strain energy per unit volume on loading and U_{UL} is the strain energy per unit volume released on unloading. The areas under the loading and unloading tensile curves were calculated by Simpson's rule. A rubber elastomer typically absorbs about 50% of the energy [37]. Loading cycles of the annealed material between $50-200$MPa, $50-250$MPa, $50-350$MPa and $50-400$MPa exhibited no hysteresis, Figure 3a - d. Loading between $50-500$MPa showed some hysteresis corresponding to 1% strain energy absorption, Figure 3e and Table 4. Between $50-600$MPa a stable hysteresis loop was observed up to 200 cycles, corresponding to $\sim$ 4% energy absorbed. The shape of the loading-unloading cycle altered with the number of cycles. It appears that the stress induced phase transformation to α'', that is responsible for the non-linearity in the elastic regime [3, 4], occurred at progressively lower stresses as cycling proceeded.

The BQ alloy had intense α'' diffraction peaks in XRD (Figure 5i), so it is lean in β-stabilising additions. The beta-quenched exhibited promising damping characteristics, with energy absorption $\sim$ 10% in the 5th cycle in both the $50-500$MPa $50-600$MPa stress ranges. However, the hysteresis loop closed and after 200 cycles the energy absorption was just 1%, while the elastic regime became more linear. The quenched microstructure is presumably highly unstable and stress-induced phase transformations that are not fully reversible stabilise the matrix, and are responsible for the changes in mechanical properties.

It is inherently difficult to determine the yield point of Ti-2448 CR and the heat-treated materials that show a smooth transition into the plastic regime and a non-linear elastic regime. In these cases the yield values presented in Table 2 were estimated. CR was not as superelastic as the annealed condition and the elastic regime was more linear, Figure 2a and b. It was far less ductile, failing after just 6% strain. The alloy became more brittle, stiff and more linear in the elastic regime with increasing ageing temperatures from 80 °C to 250 °C, Figure 2b. The CR 250 °C/24 h sample failed at yield. It was surprising that an 80 °C/24 h age diminished the mechanical properties so dramatically, so an 80 °C/750 h sample was also tested, Figure 2c. The sample was more brittle than the 80 °C/24 h heat-treated sample, failing after just 3% total strain. TEM showed clear ω diffraction spots (Figure 7), thus the reduction in ductility is associated with ω phase embrittlement [38, 39]. The CR 250 °C/24 h showed intense ω diffraction spots in TEM and the precipitation of this phase was also identified by SAXS (Figure 4 and 8), thus it can be concluded that the deterioration in mechanical properties in Ti-2448 CR with heat-treatments of $80 - 250$ °C is due to ω precipitation.

CR 450 °C/24 h exhibited a linear elastic loading response, a large increase in strength to $\sigma_y \sim 1$ GPa, but also failed at the yield point, Figure 2c. This high strength is associated with α precipitation [7]. The brittleness is an indication of ω still being present in the alloy, which is plausible as TEM has shown co-precipitation of α and ω phases in Gum Metal following a 400 °C/16 h heat-treatment [7]. A dual step heat-treatment(DHT) of Ti-2448 CR + 300 °C/24 h + 450 °C/4 h had the same stiffness as the 450 °C/24 h aged sample, but the brittle fracture occurred at a lower yield stress of 820 MPa. The lower strength is associated with the lower α ageing time.

The mechanical properties of Gum Metal were examined for comparison with the CR results. The Gum Metal had a higher yield point, which in part is due to the higher oxygen concentration [2], Table 1. The Gum Metal did not show any hysteresis on loading-unloading cycles between $50 - 500$ MPa, but did between $50 - 700$ MPa, Figure 3. However after 5 cycles the strain energy absorbed was just 1%, and this remained the case over 600 cycles.

5. Conclusions

The mechanical properties of Ti-2448 in annealed, cold-rolled, and heat-treated conditions were related to microstructural evolution using a combination of mechanical testing, SAXS, XRD and TEM.

5.1. Annealed and beta-quenched Ti-2448

XRD analysis of Ti-2448 and beta-quenched Ti-2448 showed peaks from the α'' phase, thus the material is quite lean in β-stabilising additions.

The annealed Ti-2448 exhibited non-linear loading behaviour, low elastic modulus between $16 - 48$ GPa, superelasticity, and good ductility.

Beta-quenching the material increased the non-linearity, decreased the elastic modulus to $10 - 25$ GPa and increased the superelasticity to $\sim 4\%$.

A heat-treatment of 300 °C associated with ω precipitation increased the stiffness to $48 - 64$ GPa, which is still a low modulus.

No hysteresis was observed for annealed Ti-2448 during loading-unloading cycles below maximum stresses of 500 MPa. Cycling between $50 - 600$ MPa for 200 cycles showed a stable hysteresis loop corresponding to 4% strain energy absorption. The energy absorption of Gum Metal was just 1% after 5 cycles between $50 - 700$ MPa.

The beta-quenched material initially exhibited a large hysteresis loop when cycled to both 500 MPa and 600 MPa, however the hysteresis loop closed with further cycling.

5.2. Cold-Rolled Ti-2448

The cold-rolled material was far less ductile than the annealed material. With increasing ageing temperatures from $80 - 250$ °C the elastic regime became more linear and less compliant, and the alloy became more brittle.

TEM confirmed that the material precipitated the ω phase at temperatures as low as 80 °C and this phase is well known for embrittlement [38, 39].

TEM suggests that the Ti-2448 CR material contained some α phase, while XRD showed that $alpha''$ is initially present. With low temperature ageing there is more intense diffraction from the ω and α'' phases.

SAXS modelling predicts the ω particles to be $\sim 1 - 3$ nm in size. The thermally induced change of the microstructure inhibits the β to α'' stress induced phase transformation that causes the non-linear elastic regime.

Ti-2448 CR + 450 °C/24 h increased the strength dramatically to $\sigma_y \sim 1$ GPa and brittle failure occurred at the yield point. This is indicative that co-precipitation of $\alpha + \omega$ has occurred during this heat-treatment.

In summary, α and ω precipitates are detrimental to superelasticity and hysteresis of the β-Ti alloys.

Acknowledgements

JC and MO would like to acknowledge funding provided from the Japanese Society for the Promotion of Science (JSPS). VAV and JC would like to acknowledge support from the EPSRC doctoral prize fellowship and Marie Curie fellowship respectively. Funding was also provided by EPSRC under grant EP/H0004882/0. This work made use of the J.B. Cohen X-ray Diffraction Facility at the Materials Research Center of Northwestern University supported by the National Science Foundation MRSEC program (DMR-1121262). The authors would like to thank Rui Yang for sample preparation, Shigeharu Ukai for the use of the Advanced High Temperature Laboratory at Hokkaido University, and the Imperial College London technical staff: Gary Stakalls, Russell Stracey, Simon Logsdail, Mike Lennon and Ben Wood for their continuous assistance.

References

[1] Saito T *et al.* Science 2003;300:464
[2] Obbard EG, Hao YL, Talling RJ, Li SJ, Zhang YW, Dye D, Yang R Acta Mater 2011;59:112
[3] Talling RJ, Dashwood RJ, Jackson M, Dye D. Acta Mater 2009 57:1188
[4] Liu JP *et al.* Sci Rep 2013 3:2156
[5] Ikeda M, Ueda M, Ryoichi M, Ogawa M, Niinomi M Mater Trans 2009;50(12):2737
[6] Jones NG, Talling RJ, Lindley TC, Dye D. In: L Zhou *et al.* eds., Ti2011 Science and Technology: Proceedings of the 12th World Conference on Titanium. Science Press, Beijing, China. 2012:1169–1173
[7] Coakley J, Vorontsov VA, Littrell KC, Heenan R, Ohnuma M, Jones NG, Dye D. J Alloy Compd 2015 623:146
[8] Lütjering G & Williams JC Titanium. Springer-Verlag, Berlin Heidelberg New York. 2003

[9] Nag S, Banerjee R, Srinivasan R, Hwang JY, Harper M, Fraser HL. Acta Mater 2009 57:2136
[10] Ilavsky J. J Appl. Cryst. 2012 45:324
[11] Zhang F, Ilavsky J, Long G.B, Quintana JPG. Metal. Mater. Trans. A. 2010 41A:1151
[12] Coakley J, Reed RC, Warwick JLW, Rahman KM, Dye D. Acta Mater 2012;60:2729
[13] Stone HJ, Holden TM, Reed RC. Acta Metall 1999;47:4435
[14] Ma S, Rangaswamy P, Majumdar BS. Scr Mater 2003;48:525
[15] Ma S, Brown D, Bourke MAM, Daymond MR, Majumdar BS. Mater Sci Eng A 2005;399:141
[16] Daymond MR, Preuss M, Clausen B. Acta Mater 2007;55:3089
[17] Preuss M, da Fonesca JQ, Grant B, Knoche E, Moat R, Daymond M. In: Reed RC, Green KA, Caron P, Gabb TP, Fahrmann MG, Huron ES, Woodard SA, eds., Superalloys 2008. TMS, PA, 405–414
[18] Dye D, Coakley J, Vorontsov VA, Stone HJ, Rogge RB. Scr Mater 2009;48:525
[19] Coakley J, Dye D. Scri Mater 2012;67:435
[20] King SM. In: Pethrick RA, Dawkins JV, eds., Modern techniques for polymer characterisation. Wiley, Chichester, 1999:171–232
[21] Rahman KM, Vorontsov VA, Dye D. Acta Mater 2015;89:247
[22] Mater Sci & Eng A. 2015 635:133
[23] Vorontsov VA, Jones NG, Rahman KM, Dye D Acta Mater 2015; 88:323
[24] Blackburn MJ, Feeney JA Stress-Induced Transformations in Ti-Mo Alloys. Defense Technical Information Center, 1970.
[25] Jones NG, Dashwood RJ, Jackson M, Dye D Acta Mater 2009 57:3830
[26] Jamieson JC Science 1963 146:72
[27] Settefrati A, Dehmas M, Geandier G, Denand B, Aeby-Gautier E. In: Zhou L, Chang H, Lu Y, Xu D, eds., Proceedings of the 12th World Conference on Titanium (Ti-2011). 2011:468
[28] Ho W-F Journ Med. Bio. Eng. 2008 28(1):47
[29] Takemoto Y, Shimizu i, Sakakibara A, Hida M, Mantani Y. Journ Med. Bio. Eng. 2008 28(1):47
[30] Zhou YL, Luo DM. Mater Char. 2011 62:931
[31] Song J, Zhang X, Sun X, Jiang H, Fan Z, Xie C, Wu MH. JMEPEG. 2012 21:366
[32] Ho WF, Ju CP, Lin C. Biomaterials. 1999 20:2115
[33] Xu YF, Yi DQ, Liu HQ, Wang B, Yang FL. Mater Sci & Eng A. 2011 529:326
[34] Warwick J.L.W, Coakley J, Raghunathan S.L, Talling R.J, Dye D. Acta Mater 2012;60:4117
[35] Heenan RK. RAL Report 1989;89
[36] Choe HC, Ko YM, Brantley W. NSTI-Nanotech 2008;2:454
[37] Judge AW. Aircraft and Automobile Materials of Construction. Sir Isaac Pitman & Sons, Ltd. 1921
[38] Koul MK, Breedis JF Metal Mater Trans 1970;1(5):1451
[39] Bowen AW Scripta Metal 1971;5(8):709